

Clustering, Cosmology and a New Era of Black Hole Demographics – II. The Conditional Luminosity Functions of Type 2 and Type 1 Active Galactic Nuclei

D. R. Ballantyne^{*}

Center for Relativistic Astrophysics, School of Physics, Georgia Institute of Technology, 837 State Street, Atlanta, GA 30332-0430, USA

Accepted XXX. Received YYY; in original form ZZZ

ABSTRACT

The orientation-based unification model of active galactic nuclei (AGNs) posits that the principle difference between obscured (Type 2) and unobscured (Type 1) AGNs is the line-of-sight into the central engine. If this model is correct then there should be no difference in many of the properties of AGN host galaxies (e.g., the mass of the surrounding dark matter haloes). However, recent clustering analyses of Type 1 and Type 2 AGNs have provided some evidence for a difference in the halo mass, in conflict with the orientation-based unified model. In this work, a method to compute the Conditional Luminosity Function (CLF) of Type 2 and Type 1 AGNs is presented. The CLF allows many fundamental halo properties to be computed as a function of AGN luminosity, which we apply to the question of the host halo masses of Type 1 and 2 AGNs. By making use of the total AGN CLF, the Type 1 X-ray luminosity function, and the luminosity-dependent Type 2 AGN fraction, the CLFs of Type 1 and 2 AGNs are calculated at $z \approx 0$ and 0.9. At both z , there is no statistically significant difference in the mean halo mass of Type 2 and 1 AGNs at any luminosity. There is marginal evidence that Type 1 AGNs may have larger halo masses than Type 2s, which would be consistent with an evolutionary picture where quasars are initially obscured and then subsequently reveal themselves as Type 1s. As the Type 1 lifetime is longer, the host halo will increase somewhat in mass during the Type 1 phase. The CLF technique will be a powerful way to study the properties of many AGNs subsets (e.g., radio-loud, Compton-thick) as future wide-area X-ray and optical surveys substantially increase our ability to place AGNs in their cosmological context.

Key words: galaxies: active – galaxies: haloes – quasars: general – galaxies: Seyfert – X-rays: galaxies – dark matter

1 INTRODUCTION

The unified model of active galactic nuclei (AGN) has been a central pillar of AGN phenomenology for nearly three decades. At its core, the model simply states that the central engines and environs of all AGNs are essentially the same, but, because of an axisymmetric absorbing structure (the ‘torus’), objects may have different observational properties depending on the viewing angle to the AGN (e.g., Antonucci 1993; Urry & Padovani 1995; Netzer 2015). In this way, AGNs of similar luminosities which are observed to suffer from significant line-of-sight absorption (i.e., Type 2 AGNs) differ from the unobscured, Type 1 AGNs solely due to a line-of-sight that passes through the torus. There

is substantial evidence that this orientation-based unification model is broadly applicable in local Seyfert galaxies where the nuclear regions can be studied in detail at infrared wavelengths (e.g., Burtscher et al. 2013; Hönig et al. 2013; Tristram et al. 2014). However, it is clear that this model is too simple and requires detailed adjustment to account for the wide range of obscuration properties seen at different z and luminosities (e.g., Merloni et al. 2014). For example, the fact that the fraction of obscured AGNs appears to increase with z indicates that the obscuring region is connected to the overall evolution of the host galaxy (La Franca et al. 2005; Ballantyne, Everett & Murray 2006; Treister & Urry 2006; Hasinger 2008; Ueda et al. 2014; Buchner et al. 2015). As the torus is situated at scales of 1–100 pc from the central engine, it provides a bridge between the galactic and

* E-mail: david.ballantyne@physics.gatech.edu

black hole environments, and therefore contains information on the processes responsible for fueling the nuclear activity.

An alternative to the orientation-based unified model is one based on the evolution of the sources. In this model, an event triggers luminous AGN activity that is initially obscured due to the large amount of gas funneled into the nuclear environment. Feedback from the AGN eventually clears out much of the absorbing gas and the AGN shines as a Type 1 source before fading due to the dwindling fuel supply (e.g., Sanders et al. 1988; Kauffmann & Haehnelt 2000). This evolutionary scenario has been shown to occur in numerical simulations of major merger-triggered AGNs (e.g., Hernquist 1989; Di Matteo et al. 2005; Hopkins et al. 2005). With suitable adjustment of parameters, this model can explain many aspects of AGN phenomenology (e.g., Hopkins et al. 2006, 2008). Despite this success, observations at $z \gtrsim 1$ only uncover evidence of merger triggering at the highest AGN luminosities (e.g., Kocevski et al. 2012; Treister et al. 2012; Glikman et al. 2015; Del Moro et al. 2016). Determining the redshift and luminosity range in which the orientation-based unification model holds therefore provides crucial information on the triggering mechanisms of these AGNs. Regions in the redshift-luminosity plane where the unified model fails are more likely to be subject to the drastic fueling events needed for the evolutionary scenario.

Since the orientation-based unified model states that the main difference between Type 2 and Type 1 AGNs is the view through the parsec-scale obscuring torus, the galactic environment of AGN host galaxies should be independent of the level of nuclear obscuration. One way to quantitatively test this prediction is to measure the clustering properties (such as the average AGN bias, \bar{b}_A , or mean dark matter halo mass, $\langle M_h \rangle$), of both Type 1 and Type 2 AGNs. In the orientation-based unification model, these quantities should be similar for both populations. Performing this test is challenging because large samples of both types of AGNs need to be identified over wide areas. However, recently several groups have utilized large *Spitzer* and *WISE* IR-selected samples of quasars to investigate the clustering properties of Type 1 and 2 AGNs at $z \sim 1$. After separating the two classes by an optical/IR colour cut, some authors found that obscured AGNs were more biased and thus populated more massive haloes than unobscured ones (e.g., Hickox et al. 2011; Donoso et al. 2014; DiPompeo et al. 2014; DiPompeo, Hickox & Myers 2016), with a difference in halo mass ranging from a factor of 2 to 10. The statistical significance of the difference also varies greatly from study to study, and indeed other groups report no difference between the two types (Geach et al. 2013; Mendez et al. 2016). Interestingly, Allevato et al. (2011, 2014) used X-ray selected AGNs in the COSMOS field and found the opposite tendency at $z \sim 2$ and 3; that is, Type 1 AGNs were more biased and inhabited more massive haloes than obscured AGNs (see also Cappelluti et al. 2010). Direct comparison between the X-ray and IR results is problematic due to the strong selection effects that arise from constructing each sample (Mendez et al. 2016). Nevertheless, there are now several results indicating that Type 1 and 2 AGNs may inhabit different environments, in contrast to the orientation-dependent unification picture.

These recent observational results probe only certain

AGN luminosities, but if the lower-luminosity Seyfert galaxies are likely triggered by different processes than quasars (e.g., Draper & Ballantyne 2012) the nature of AGN obscuration could change with luminosity. While performing clustering analyses of Type 1 and 2 AGNs in narrow luminosity bins is not possible with current data, future wide-field surveys by *eROSITA*, *Euclid*, *WFIRST* and LSST will allow this experiment. In preparation for this new era of AGN demographics Ballantyne (2016; hereafter Paper I), presented a method to compute the Conditional Luminosity Function (CLF) of AGNs using X-ray survey data. The CLF allows the computation of multiple statistics of how AGNs populate dark matter haloes as a function of luminosity. Paper I computed the CLF at both $z \approx 0$ and ≈ 0.9 and showed that the mean halo mass of AGNs does increase with luminosity at both epochs, indicating how the fueling of AGNs differs with luminosity and z .

In this paper, the X-ray CLF methodology developed in Paper I is modified so that CLFs of Type 1 and Type 2 AGNs can be individually constrained at $z \approx 0$ and 0.9 (Sects. 2 and 3). The CLF-derived statistics on the host halo properties of Type 2 and Type 1 AGNs are described in Sect. 4. The implications of these results on the AGN unification model and triggering physics are discussed and summarized in Section 5. As in Paper I, a WMAP9 Λ CDM cosmology is assumed in this work: $h = 0.7$, $\Omega_m = 0.279$, $\Omega_\Lambda = 0.721$ and $\sigma_8 = 0.821$ (Hinshaw et al. 2013).

2 THE CONDITIONAL LUMINOSITY FUNCTION OF TYPE 2 AND TYPE 1 AGNS

This section first gives a brief overview of the key definitions and equations behind the AGN CLF methodology presented in Paper I. This method closely follows the CLF model for galaxies first described by Yang et al. (2003) and van den Bosch et al. (2003). The description is first focused on the entire AGN population, and then Sect. 2.2 presents how to break down the total CLF to ones for the Type 2 and Type 1 AGN population.

2.1 Brief Review of CLF Definitions

The AGN CLF, $\Psi(L|M_h)$, is defined at a specific z so that the XLF is obtained when the CLF is integrated over all halo masses; i.e.,

$$\phi(L) = \int_0^\infty \Psi(L|M_h) n(M_h) dM_h, \quad (1)$$

where $\phi(L) = d\Phi/d\log L$ is the AGN XLF in a specific energy band (here, 2–10 keV), and $n(M_h)$ is the dark matter halo mass function. A crucial aspect of the CLF is that it provides a statistical description of how AGNs of different luminosities are distributed in halos of various masses. Therefore, once constrained the CLF can be used to calculate several statistical measures of the AGN population, such as the mean number of AGNs with luminosities between L_1 and L_2 as a function of halo mass, M_h :

$$\langle N(M_h) \rangle = \int_{L_1}^{L_2} \Psi(L|M_h) dL. \quad (2)$$

From this, the average M_h hosting an AGN with a luminosity in this interval of L is (Yang et al. 2003)

$$\langle M_h(L) \rangle = \frac{1}{\phi(L)} \int_0^\infty M_h \langle N(M_h) \rangle n(M_h) dM_h. \quad (3)$$

The CLF can also be used to estimate the lifetime of AGNs by following the argument of Martini & Weinberg (2001). Paper I showed that the AGN lifetime as a function of luminosity can be estimated as

$$\tau_{\text{AGN}}(L) = \langle \Psi(L | M_h(L)) \rangle dL \tau_{\text{Hubble}}, \quad (4)$$

where τ_{Hubble} is the Hubble time at the redshift of interest. Indeed, all of the above expressions are evaluated at a specific z , but the z -dependence is not included for the sake of clarity.

As it is a statistical description of the AGN population in the cosmological environment, the CLF must be parameterized and constrained by observational data instead of being derived from a fundamental theory. Paper I showed that the following parameterization of the CLF was appropriate for AGNs at $z \approx 0$ and ≈ 0.9 :

$$\Psi(L|M_h) = \left(\frac{M_h}{M_*} \right)^a e^{-M_h/M_{\text{cut}}} f(L) \quad (5)$$

where

$$M_{\text{cut}} = \left(\frac{L}{L_*} \right)^c M_N, \quad (6)$$

and

$$f(L) = \begin{cases} \left(\frac{L}{L_*} \right)^{-0.96} & \text{if } L < L_* \\ \left(\frac{L}{L_*} \right)^{-\beta} & \text{otherwise.} \end{cases} \quad (7)$$

This form for the CLF has 6 free parameters (a , M_* , β , L_* , c , and M_N) and was chosen to give a broken power-law XLF and a cutoff power-law $\langle N(M_h) \rangle$, both consistent with observations (e.g., Ueda et al. 2014; Leauthaud et al. 2015).

Following Yang et al. (2003), Paper I used the observed AGN XLF plus measurements of the AGN correlation length at different luminosities, $r_0(L)$, to constrain the CLF parameters. The correlation lengths, defined as the radius where the AGN two-point correlation function, $\xi_{\text{AA}}(r)$ is unity, are typically large enough that the ‘2-halo’ contribution dominates the correlation function. The ‘2-halo’ component describes the clustering of AGNs hosted in separate dark matter haloes, and is related to the clustering of the haloes themselves,

$$\xi_{\text{AA}}^{2h}(r) \approx \bar{b}_A^2 \xi_{\text{dm}}^{2h}, \quad (8)$$

where ξ_{dm}^{2h} is the ‘two-halo’ contribution to the total dark matter correlation function (defined as $\xi_{\text{dm}}^{2h} = \xi_{\text{dm}} - \xi_{\text{dm}}^{1h}$), and

$$\bar{b}_A = \frac{\int_0^\infty n(M_h) \langle N(M_h) \rangle b(M_h) dM_h}{\int_0^\infty n(M_h) \langle N(M_h) \rangle dM_h} \quad (9)$$

is the mean AGN bias ($b(M_h)$ is the bias of dark matter haloes to the dark matter distribution). As ξ_{dm}^{2h} and $b(M_h)$ can be computed from a cosmological model, the CLF allows \bar{b}_A and $\xi_{\text{AA}}^{2h}(r)$ to be calculated for different luminosity ranges. As before, these quantities are also functions of z . The Tinker et al. (2010) fitting formulas for $n(M_h)$ and $b(M_h)$ are used in the calculations, and further information on the cosmological details needed in the CLF modeling can be found in Appendix A of Paper I.

2.2 Determining the Type 2 and Type 1 CLFs

In Paper I, the AGN CLF was constrained at $z \approx 0$ and 0.9 and the above statistical measurements of the total AGN population were examined at these two redshifts. van den Bosch et al. (2003) showed how the total CLF of galaxies could be separated into ones for early-type and late-type galaxies. Here, the method of van den Bosch et al. (2003) is adapted in order to determine the CLFs for Type 2 and Type 1 AGNs. Once known, the equations from Sect. 2.1 can be used to calculate statistics for each set of AGNs.

We begin by noting that the AGN CLF can be decomposed into the sum of the CLF for Type 2 AGNs, $\Psi(L|M_h)_2$, and the CLF for Type 1 AGNs, $\Psi(L|M_h)_1$; i.e.,

$$\Psi(L|M_h) = \Psi(L|M_h)_1 + \Psi(L|M_h)_2. \quad (10)$$

In the case considered here and in Paper I, the above statement is true for Compton thin AGNs, as the number of Compton thick sources are negligible in the samples used to constrain the CLFs.

By defining $f_2(L, M_h)$ as the fraction of Type 2 AGNs with luminosity L in haloes of mass M_h , the Type 2 and Type 1 CLFs can be written as

$$\Psi(L|M_h)_2 dL = f_2(L, M_h) \Psi(L|M_h) dL \quad (11)$$

and

$$\Psi(L|M_h)_1 dL = (1 - f_2(L, M_h)) \Psi(L|M_h) dL. \quad (12)$$

Integrating $f_2(L, M_h)$ over mass or luminosity gives the mean AGN Type 2 fraction as a function of luminosity or mass, respectively; i.e.,

$$\bar{f}_2(L) = \frac{\int f_2(L, M_h) \Psi(L|M_h) n(M_h) dM}{\int \Psi(L|M_h) n(M_h) dM} \quad (13)$$

and

$$\bar{f}_2(M_h) = \frac{\int f_2(L, M_h) \Psi(L|M_h) dL}{\int \Psi(L|M_h) dL} \quad (14)$$

The left hand side of Eq. 13 can be measured observationally, but the exact dependence of the Type 2 fraction with luminosity is much debated (Burlon et al. 2011; Merloni et al. 2014; Sazonov, Churazov & Krivonos 2015).

To determine $f_2(L, M_h)$, we again follow van den Bosch et al. (2003) and assume it is separable; i.e., $f_2(L, M_h) = g(L)h(M_h)$ (this assumption is checked in Appendix A). With this assumption $g(L)$ can be written as

$$g(L) = \bar{f}_2(L) \frac{\int \Psi(L|M_h) n(M_h) dM}{\int \Psi(L|M_h) h(M_h) n(M_h) dM} \quad (15)$$

Thus, since $\bar{f}_2(L)$ is observed for AGNs, if $h(M_h)$ can be constrained, $g(L)$ and hence $f_2(L, M_h)$, $\Psi(L|M_h)_2$, and $\Psi(L|M_h)_1$ all can be determined. Once the individual CLFs are known, they can be used to calculate all the standard CLF-derived statistics described in Sect. 2.1 for both Type 2 and Type 1 AGNs.

3 APPLICATION TO AGNS AT $Z \approx 0$ AND 0.9

The decomposition of the AGN CLF into the sum of the Type 2 and Type 1 CLFs requires first knowing the total CLF at the redshift of interest. In Paper I, the total AGN

CLF was determined at $z \approx 0$ and $z \approx 0.9$. Now, these CLFs will be used along with estimates of $f_2(L)$ to derive individual CLFs for Type 2 and 1 AGNs at both redshifts.

As in Paper I, an AGN XLF will be used to constrain the CLFs. Here, we make use of the Type 1 XLFs determined by [Hasinger, Miyaji & Schmidt \(2005\)](#) using AGNs selected in the 0.5–2 keV band (the XLFs are converted to the 2–10 keV band employed here using the same procedure and spectral model as [Ballantyne \(2014\)](#)). The Type 1 AGNs used to measure the XLFs were identified by the presence of broad Balmer lines in the optical spectrum or X-ray hardness ratios. There is generally good agreement between the optical and X-ray definitions of Type 1 and 2 AGNs (e.g., [Hasinger 2008](#); [Merloni et al. 2014](#); [Burtscher et al. 2016](#)); thus, we make use of X-ray determined $f_2(L)$ estimates at $z \approx 0$ ([Burlon et al. 2011](#)) and 0.9 ([Merloni et al. 2014](#)). The [Burlon et al. \(2011\)](#) study of *Swift*-BAT-detected AGNs is hard X-ray selected and shows the least bias for detecting Compton-thin AGNs (but see [Sazonov et al. 2015](#)). [Burlon et al. \(2011\)](#) found that the fraction of obscured AGNs (defined as those with column densities $> 10^{22} \text{ cm}^{-2}$) could be described as

$$f_2^{z \approx 0}(L) = 0.8e^{-L/10^{43.7}} + 0.2(1 - e^{-L/10^{43.7}}), \quad (16)$$

where the L is defined in the 15–55 keV band (we assume the same form for the 2–10 keV band, as the changes in luminosities between the two bands are relatively small). There is some evidence that the Type 2 fraction increases with z , especially at $\log(L/\text{erg s}^{-1}) \gtrsim 44$ (e.g., [Ueda et al. 2014](#)). To capture this effect, Eq. 16 is revised so that the Type 2 fraction roughly follows the $z \approx 0.9$ estimates of [Merloni et al. \(2014\)](#):

$$f_2^{z \approx 0.9}(L) = 0.75e^{-L/10^{44.2}} + 0.5(1 - e^{-L/10^{44.2}}). \quad (17)$$

The procedure to determine $\Psi(L|M_h)_2$, and $\Psi(L|M_h)_1$ at each z is as follows. For a specific parameterization of $h(M_h)$, the total AGN CLF from Paper I is used along with the appropriate $f_2(L)$ to compute $g(L)$ (Eq. 15). Then $f_2(L, M_h) = g(L)h(M_h)$ is determined while enforcing the condition that $f_2(L, M_h) \leq 1$ for all L and M_h . The Type 1 AGN CLF, $\Psi(L|M_h)_1$, is then calculated (Eq. 12), and from that the Type 1 XLF can be computed (Eq. 1) and compared to the observed datapoints. As in Paper I, a χ^2 is computed and the [Metropolis et al. \(1953\)](#) algorithm is used to adjust any $h(M_h)$ parameters in order to minimize the χ^2 calculated from Type 1 XLF. There are 19 datapoints defining the $z \approx 0$ Type 1 XLF and 11 for the one at $z \approx 0.9$. However, the $z \approx 0.9$ Type 1 XLF contains AGNs between $z = 0.8$ and 1.6, and the two highest luminosity points (which would be most heavily influenced by AGNs at higher z) predicted space densities larger than the total [Ueda et al. \(2014\)](#) XLF at $z \approx 0.9$. Therefore, we omit these two points when determining the CLFs.

After many trials it was found that the simple form $h(M_h) = e^{-M_h/M_*}$, where M_* is the only parameter, provides the best fit to the XLFs for these forms of $f_2(L)$. More complex forms of $h(M_h)$ did not significantly improve the fits to the XLFs, but may be required for different forms of $f_2(L)$ or for different XLF shapes. The resulting values of M_* and the χ^2 obtained are shown in Table 1. Initially, the minimum reduced χ^2 at $z \approx 0$ was > 2 , largely due to the small error-bars and wiggles in the published XLF. Increasing the error-bars

Table 1. Results of fitting the [Hasinger et al. \(2005\)](#) Type 1 XLF using the total AGN CLF from Paper I, $f_2(L)$ (either Eq. 16 or 17), and assuming $h(M_h) = e^{-M_h/M_*}$. The error-bars are calculated using a $\Delta\chi^2 = 2.71$ criterion (i.e., a 90% confidence level for the parameter of interest). Due to the small error-bars and some wiggles in the published XLF, the error-bars of the $z \approx 0$ XLF are increased by 40% to lower the minimum reduced χ^2 to 1.2 (there is no change in the fit parameter). No upper-bound on M_* was obtained at $z \approx 0$ (the maximum $\Delta\chi^2$ in that direction was 1.28).

Redshift	χ^2/dof	$\log(M_*/M_\odot)$
0	21.4/18	$13.97^{+2}_{-0.31}$
0.9	9.8/8	$14.17^{+0.45}_{-0.19}$

by 40% lowered the minimum reduced χ^2 to 1.2 with no change in the fit parameter. At $z \approx 0.9$, the reduced χ^2 is 1.2, so no changes were needed to the published error-bars. The best value of $\log M_*$ is larger at $z \approx 0.9$ than at $z \approx 0$, although they are consistent within the errorbars (defined as the 90% confidence level for one degree of freedom; i.e., a $\Delta\chi^2 = 2.71$ criterion). However, an upper error-bar could not be found at that confidence level at $z \approx 0$ (the maximum $\Delta\chi^2$ obtained in that direction is 1.28). This is because the CLF model associates high mass haloes with high luminosity AGNs (Paper I), and the fraction of Type 2 AGNs at quasar luminosities at $z \approx 0$ is small enough that there is little sensitivity to how the Type 2 AGNs are distributed in haloes with $M_h > M_*$.

Figure 1 plots the predicted Type 2 and Type 1 XLFs at both redshifts derived from the best-fit CLF models. The [Hasinger et al. \(2005\)](#) Type 1 XLF that was used to constrain the CLF is shown as the solid points in both panels. In addition, the $z \approx 0$ Type 2 XLF measured by [Burlon et al. \(2011\)](#) using *Swift*-BAT is shown as the open stars in the left-hand panel of Fig. 1. These data were not used to help constrain the Type 2 CLF as they are not independent from the $f_2(L)$ measurement, but it is clear that the CLF-derived Type 2 XLF provides an excellent description of the data at this z . The right-hand panel also plots (as open stars) the [Ueda et al. \(2014\)](#) $z = 0.9$ Type 2 XLF calculated by multiplying their total XLF data with their prescription for $f_2(L)$ (their Eq. 3). The CLF-derived Type 2 XLF at $z \approx 0.9$ is consistent with the [Ueda et al. \(2014\)](#) data despite the different assumed forms of $f_2(L)$ and our use of the [Hasinger et al. \(2005\)](#) data to constrain the XLFs. This agreement indicates that our procedure produces a $\Psi(L|M_h)_2$ and $\Psi(L|M_h)_1$ that is self-consistent with the underlying total CLF computed in Paper I.

The hatched regions in Fig. 1 are the 95% confidence regions of the derived XLFs, calculated using a similar Monte-Carlo method described in Paper I. Briefly, starting from its best-fit value M_* is randomly varied, and a χ^2 is calculated. If this χ^2 is within the 95% confidence region for one degree of freedom (a $\Delta\chi^2 \leq 3.84$ criterion) the value of M_* is stored. After 300 random changes, M_* is reset to the best-fit value, and the process restarts until a total of 3000 changes have been considered. To take into account the uncertainty in the total AGN CLF, the above procedure is performed 10 times: once with the best-fitting CLFs from Paper I, and nine other times with the six CLF parameters randomly varied within their 90% errorbars (see Table 1 in Paper I). After comple-

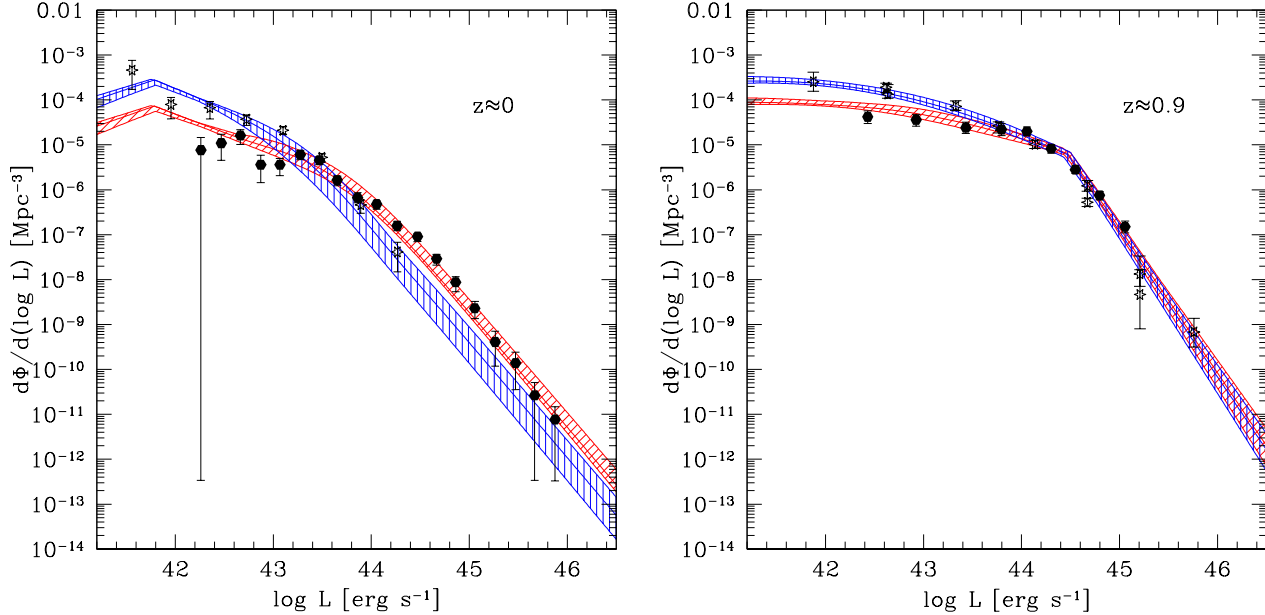


Figure 1. (Left) The predicted 2–10 keV Type 2 (blue lines and hatched region) and Type 1 (red lines and hatched region) AGN XLFs computed at $z \approx 0$ from the best fit CLFs (Eqs. 11 and 12). The solid points are from the [Hasinger et al. \(2005\)](#) measurement of the Type 1 AGN XLF translated to the 2–10 keV band using the procedure of [Ballantyne \(2014\)](#). The open stars are the Type 2 XLF measured by [Burlon et al. \(2011\)](#) using *Swift*-BAT (also converted to the 2–10 keV band). The CLFs were constrained by only fitting the Type 1 XLF, but clearly do an excellent job describing the Type 2 XLF at this z . The hatched regions denote the 95% confidence levels of the predicted XLFs (see text for details). (Right) As in the left-hand panel, but now showing the predicted XLFs at $z \approx 0.9$. The solid points are the Type 1 AGN XLF as measured by [Hasinger et al. \(2005\)](#) at $z = 0.8 - 1.6$, after omitting the two highest luminosity points. The open stars plot the $z = 0.9$ Type 2 AGN XLF calculated from the [Ueda et al. \(2014\)](#) XLF data using their $f_2(L)$ prescription (their Eq. 3). The CLF-derived Type 2 XLF remains consistent with the [Ueda et al. \(2014\)](#) XLF.

tion, a total of 3958 (5841) CLF models for $z \approx 0(0.9)$ within the confidence region are stored. These are then searched to find the minimum and maximum values of the quantity of interest as a function of luminosity or halo mass. The confidence regions are then defined as the space between the maxima and minima and are shown in all future plots.

4 RESULTS

In this section, the CLF-derived statistics are used to determine if there is a significant difference in dark matter halo properties of obscured and unobscured AGNs.

Before using the individual Type 2 and Type 1 AGN CLFs to derive population statistics, it is illuminating to use Eq. 14 to simply calculate how the mean fraction of Type 2 AGNs depends on M_h . The thin solid line in Fig. 2 shows that at both redshifts the mean Type 2 fraction seems to depend significantly on halo mass when $\log(M_h/M_\odot) \gtrsim 13$. However, it is important to recognize that some dependence of the mean Type 2 fraction on M_h is expected because of two observational facts: first, the Type 2 fraction drops at high AGN luminosities (Eqs. 16 & 17), and, second, the correlation length increases with luminosity indicating that high luminosity AGNs are found in higher mass haloes ([Cappelluti et al. 2010](#); [Koutoulidis et al. 2013](#); Paper I). Thus, a smaller Type 2 fraction is expected at high halo masses regardless of the clustering properties of the two populations. To illustrate this, the thick black lines in both

panels show $\bar{f}_2(M_h)$ in the situation where the bias, M_h and other clustering properties of Type 1 and 2 AGNs are identical (operationally, this is computed by setting M_* to a very large value in $h(M_h)$). These curves overlap with the boundary of the 95% confidence regions of $\bar{f}_2(M_h)$ computed from our CLF procedure (red lines). Therefore, it appears that at both $z \approx 0$ and 0.9, there is only very weak evidence for a difference in the host halo properties of Type 1 and 2 AGNs.

To see this explicitly, Eqs. 9 and 3 are used to compute the average AGN bias, \bar{b}_A , and mean halo mass as a function of AGN luminosity, $\langle M_h \rangle(L)$, directly from the Type 1 and Type 2 CLFs at both z . The resulting values, and their corresponding 95% confidence regions are plotted in Figs. 3 and 4. All of the $\langle M_h \rangle(L)$ and \bar{b}_A curves exhibit moderate to strong luminosity dependence with larger values expected at $\log(L/\text{erg s}^{-1}) \gtrsim 44$. This behaviour is a direct result of the total AGN CLF derived from Paper I that was used in the calculation, and shows that high and low luminosity AGNs of both types likely inhabit different environments. Paper I discusses that this evolution in luminosity is a strong indication that the triggering physics is different in the two luminosity regimes.

In this paper, our focus is on any differences between the Type 2 and Type 1 AGNs. Figs. 3 and 4 show that the confidence regions of the two types overlap at all luminosities for both z . Therefore, as expected from the $f_2(M_h)$ results, there is no significant difference in the mean halo mass or bias between the two populations. The predictions of the CLF model (solid lines) appear to indicate a separa-

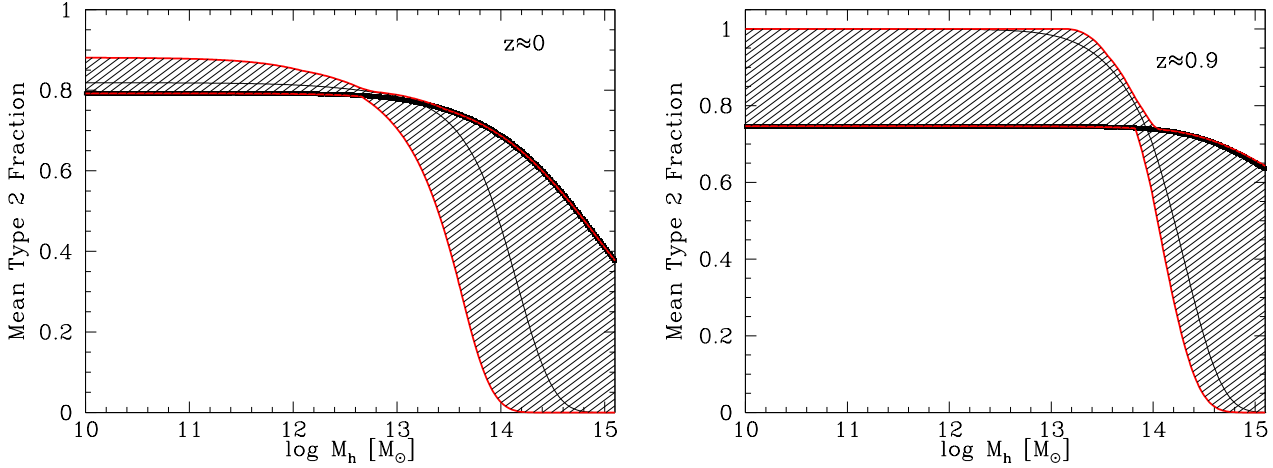


Figure 2. (Left) The thin solid line plots the mean Type 2 AGN fraction as a function of halo mass at $z \approx 0$ as derived from the AGN CLF (Eq. 14). The hatched region indicates the 95% confidence region. The thick black line is the expected variation in the mean Type 2 fraction when there is *no difference* in the halo or clustering properties between Type 1 and Type 2 AGN. As this line is consistent with the boundary of the 95% confidence region (red lines), there is only marginal evidence for a difference in the mean Type 2 fraction at $z \approx 0$. (Right) As in the left-hand panel, but at $z \approx 0.9$. Similar to the situation at lower redshift, the predicted variation in the mean Type 2 fraction with M_h is not significantly different from the one expected when obscured and unobscured AGNs have identical clustering properties.

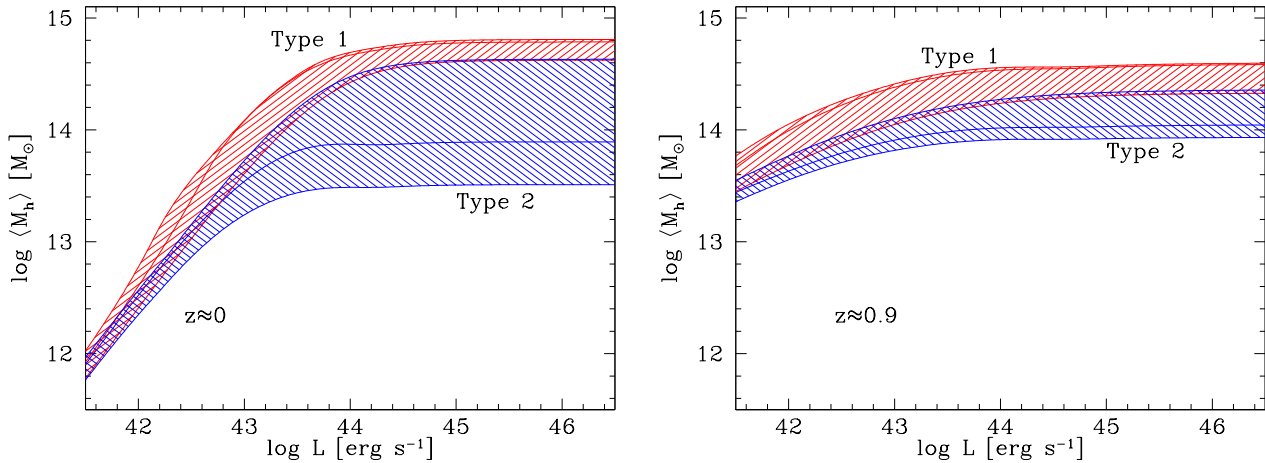


Figure 3. The CLF-derived Type 2 (blue) and Type 1 (red) AGN mean halo mass, $\langle M_h \rangle$, as a function of AGN X-ray luminosity at $z \approx 0$ (Left) and $z \approx 0.9$ (Right). The solid lines are the values predicted by Eq. 3, and the surrounding hatched areas are the 95% confidence regions. The luminosity dependence in both quantities follows from the form of the total AGN CLFs derived in Paper I. At both redshifts, there is marginal evidence that Type 1 AGNs inhabit more massive haloes than Type 2 AGNs, in particular at $\log(L/\text{erg s}^{-1}) \gtrsim 43\text{--}44$. However, the fact that the confidence regions overlap indicates that the difference in halo mass is not significant. The halo masses for $z \approx 0$ Type 1 quasars are likely overestimated due to limitations with the available data when deriving the total CLF (Paper I). The $z \approx 0$ Type 2 confidence region is substantially larger than the one for Type 1 AGNs because of the unconstrained upper-limit on M_* (Table 1).

tion between the populations, in particular at higher luminosities. This is marginal evidence that Type 1, unobscured quasars, are more biased and inhabit more massive haloes than obscured, Type 2, quasars. Interestingly, the sense of the difference in halo mass agrees with the other X-ray based results (Allevato et al. 2011, 2014) at much higher z . Lower-luminosity Seyfert galaxies, in contrast, appear more likely to have the same \bar{b}_A and $\langle M_h \rangle$ for both Type 2 and Type 1 AGNs, as expected for the orientation-based model. Indeed, it is these types of AGNs in which observations can directly probe the nature of any torus-like structure (e.g., Burtcher et al. 2013).

5 DISCUSSION AND SUMMARY

The question of whether or not the orientation-based unification model is valid at all AGN luminosities and redshifts is important for constructing the correct model of black hole growth and galaxy evolution. A potentially clear approach to this problem that avoids interpreting the complex radiative environment around the AGN is to measure the halo masses of the host galaxies of both obscured and unobscured AGNs. If the orientation-based unification model holds the host haloes should be independent of the nuclear obscuration properties.

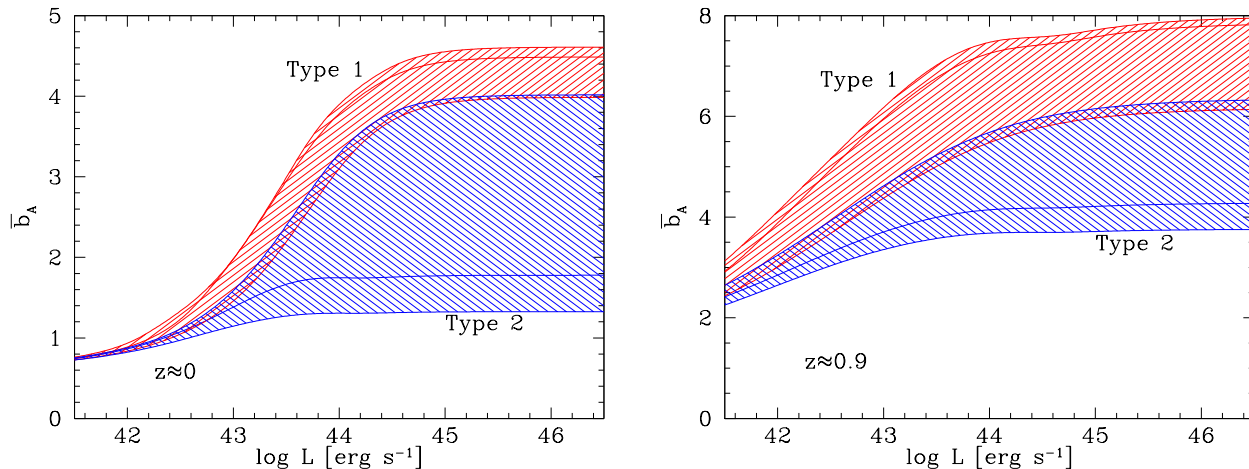


Figure 4. The CLF-derived Type 2 and Type 1 mean AGN bias, \bar{b}_A , as a function of AGN X-ray luminosity at $z \approx 0$ (Left) and $z \approx 0.9$ (Right). The solid lines are the values predicted by Eq. 9, and the surrounding hatched areas are the 95% confidence regions. As with $\langle M_h \rangle$, the luminosity dependence in both quantities follows from the form of the total AGN CLFs derived in Paper I. Also similar to the mean halo mass, the confidence regions of \bar{b}_A overlap at all luminosities indicating that any difference in average bias is not significant. As in Fig. 3, the undetermined upper-limit to M_* leads to a larger uncertainty in the predicted bias of Type 2 AGNs at $z \approx 0$.

Building on earlier work on the clustering of galaxies (e.g., Yang et al. 2003), Paper I presented a method to measure the AGN CLF at a particular redshift. With the CLF several statistics of the host haloes of AGNs can be computed as a function of luminosity, including the bias, mass, and AGN occupation numbers. In this paper, we showed how the total AGN CLF can be decomposed into ones describing Type 1 and Type 2 AGNs, and therefore the mean halo masses of both populations can be computed as a function of luminosity at specific redshifts. Using measurements of the Type 1 XLF by Hasinger et al. (2005) and estimates of the luminosity dependent Type 2 fraction $f_2(L)$ (Burlon et al. 2011; Merloni et al. 2014), the Type 1 and 2 CLFs were constrained at $z \approx 0$ and 0.9. However, there was no statistically significant difference in the mean halo mass, $\langle M_h \rangle(L)$, between Type 1 and 2 AGNs at either z (Fig. 3). The uncertainty in the predicted $\langle M_h \rangle(L)$ is significant, so the addition of further data is needed to more precisely test if Type 1 and 2 AGNs inhabit haloes of similar masses at all luminosities. The most useful data for this purpose would be measurements of the correlation length at different AGN luminosities, $r_0(L)$, for at least one of the AGN types. In the X-ray band, such data may have to await for the surveys performed by *eROSITA*.

Although the results are not significant, it is interesting to consider the interpretation of the prediction shown in Fig. 3; namely, that the host galaxies of Type 1 AGNs inhabit more massive haloes than Type 2 AGN host galaxies, particularly at $\log(L/\text{erg s}^{-1}) \gtrsim 43$. As mentioned in Sect. 1, an alternative to the orientation-based unification model is one where AGNs evolve from an obscured phase to an unobscured phase. In this scenario, unobscured Type 1 quasars observed at, e.g., $z \approx 0.9$ were triggered earlier and are at a different point in their evolution than the obscured Type 2 quasars observed at the same redshift. As this Type 1 phase lasts longer than the obscured phase (e.g., Hopkins et al. 2008) then Type 1 quasars will be more frequently observed at a specific z . Furthermore, as the Type 1s were triggered

earlier than the Type 2s, the dark matter halo hosting the Type 1 AGN will have accreted additional mass prior to being observed. Thus, even if quasars are triggered in haloes with a narrow range of masses (e.g., Hickox et al. 2009), the evolutionary model predicts that obscured and unobscured AGNs will appear to reside in different haloes when compared at the same z . For example, using Eqn. 2 from Fakhouri, Ma & Boylan-Kolchin (2010) a $10^{14} M_\odot$ halo at $z \sim 1$ will accrete $\approx 2 \times 10^{13} M_\odot$ in the $\sim \text{Gyr}$ timescale of the fading Type 1 quasar (Hopkins et al. 2006). Such a change would be challenging to detect at $z \lesssim 1$, but might be possible at higher redshifts when the halo accretion rates are larger (cf., Allevato et al. 2011, 2014). Our CLF results are consistent with this small change, but larger differences are possible which, if confirmed by revising the CLF fits with improved data, would lead to a substantial revision to our understanding of AGN physics.

As a check on these ideas, Fig. 5 plots the estimated AGN Type 1 and Type 2 lifetimes at $z \approx 0.9$ computed from the CLFs (via Eq. 4). These lifetimes are estimated from the ratio of the AGN space density to the dark matter halo density (Martini & Weinberg 2001), and are therefore difficult to directly compare to the predictions of, for example, merger-triggered AGN evolution where the luminosity of an AGN varies significantly over its lifetime (e.g., Hopkins et al. 2008). Nevertheless, this snapshot of the AGN population at $z \approx 0.9$ shows an interesting evolution across luminosity that can be explored in future work. The figure shows that, although the confidence regions formally overlap at all luminosities, the overlap is smallest at $\log(L/\text{erg s}^{-1}) \gtrsim 44$. Below that luminosity, Type 1 and 2 AGNs appear to have similar lifetimes, but above $\log(L/\text{erg s}^{-1}) \sim 44$ the Type 1 lifetime may be larger, and last hundreds of Myrs, consistent with the evolutionary model described above.

Observationally, differences in the host halo masses of Type 1 and 2 AGNs have been typically been very small (DiPompeo et al. 2016), or non-existent (Mendez et al. 2016). Interestingly, the studies that have found that unob-

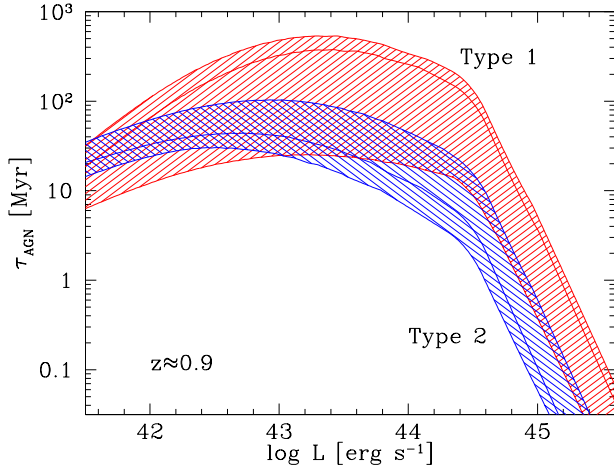


Figure 5. The CLF-derived Type 2 and Type 1 AGN lifetimes, τ_{AGN} , as a function of AGN X-ray luminosity at $z \approx 0.9$. The solid lines are the values predicted by Eq. 4, and the surrounding hatched areas are the 95% confidence regions. Although, again, the results are not significant, there are indications that at $\log(L/\text{erg s}^{-1}) \gtrsim 44$ the lifetimes of Type 1 AGNs are longer than Type 2s and can last several hundreds of Myrs, consistent with the evolutionary picture of AGNs.

scured AGNs have larger halo masses than Type 2 objects use exclusively X-ray selected samples (Allevato et al. 2011, 2014). Analyses that find the opposite trend (haloes hosting obscured AGN are more massive) often utilize IR selected AGN samples. As emphasized by Mendez et al. (2016), the different wavelengths select different types of host galaxies, and, since the size of the true effect may be small, its not clear if the two sets of measurements represent a fundamental disagreement. For example, a substantial fraction of the infrared AGNs are so cocooned by gas and dust that they would be undetected in X-ray surveys (e.g., Donoso et al. 2014). Therefore, studies based on these samples may be selecting a specific time in AGN evolution. The CLF-derived results presented here make use of X-ray selected AGNs, and the trend we uncover is consistent with the previously mentioned X-ray results.

Finally, it is worth noting that the method described in Sect. 2 can be applied to any subset of AGNs with which there are appropriate datasets. For example, individual CLFs for radio-loud and radio-quiet AGNs, or Compton-thick and Compton-thin AGNs could be derived using this procedure. Data produced from future surveys by *eROSITA*, *LSST*, *Euclid*, *WFIRST* and *Athena* can then be exploited to provide a comprehensive view of multiple facets of the AGN phenomenon and how it connects to the overall cosmic web.

ACKNOWLEDGMENTS

The author thanks J. Wise, G. Altay, A. Myers, and R. Grissom for help and advice during the course of this work, R. Hickox for comments on a draft of the manuscript, and acknowledges support from NSF award AST 1333360.

REFERENCES

- Allevato V., et al., 2011, *ApJ*, 736, 99
 Allevato V., et al., 2014, *ApJ*, 796, 4
 Antonucci R., 1993, *ARA&A*, 31, 473
 Ballantyne D.R., 2014, *MNRAS*, 437, 2845
 Ballantyne D.R., 2016, *MNRAS*, submitted (Paper I)
 Ballantyne D.R., Everett J.E., Murray N., 2006, *ApJ*, 639, 740
 Buchner J., Georgakakis A., Nandra K., Brightman M., Menzel M.-L., Liu Z., Hsu L.-T., Salvato M., Rangel C., Aird J., Merloni A., Ross N., 2015, *ApJ*, 802, 89
 Burlon D., Ajello M., Greiner J., Comastri A., Merloni A., Gehrels N., 2011, *ApJ*, 728, 58
 Burtscher L., et al., 2013, *A&A*, 558, 149
 Burtscher L., et al., 2016, *A&A*, 586, A28
 Cappelluti N., Ajello M., Burlon D., Krumpke M., Miyaji T., Bonoli S., Griener, J., 2010, *ApJ*, 716, L209
 Cappelluti N., Allevato V., Finoguenov, A., 2012, *Adv. in Astron.*, 853701
 Del Moro A., et al., 2016, *MNRAS*, 456, 2105
 Di Matteo T., Springel V., Hernquist L., 2005, *Nature*, 433, 604
 DiPompeo M.A., Myers A.D., Hickox R.C., Geach J.E., Hainline K.N., 2014, *MNRAS*, 442, 3443
 DiPompeo M.A., Hickox R.C., Myers A.D., 2016, *MNRAS*, 456, 924
 Donoso E., Yan L., Stern D., Assef R., 2014, *ApJ*, 789, 44
 Draper A.R., Ballantyne D.R., 2012, *ApJ*, 751, 72
 Fakhouri O., Ma C.-P., Boylan-Kolchin M., 2010, *MNRAS*, 406, 2267
 Geach J.E., et al., 2013, *ApJ*, 776, L41
 Glikman E., Simmons B., Maily M., Schawinski K., Urry C.M., Lacy, M., 2015, *ApJ*, 806, 218
 Hasinger G., 2008, *A&A*, 490, 905
 Hasinger G., Miyaji T., Schmidt M., 2005, *A&A*, 441, 417
 Hernquist L., 1989, *Nature*, 340, 687
 Hickox R.C., et al., 2009, *ApJ*, 696, 891
 Hickox R.C., et al., 2011, *ApJ*, 731, 117
 Hinshaw G., et al., 2013, *ApJS*, 208, 19
 Hönig S.F., et al., 2013, *ApJ*, 771, 87
 Hopkins P.F., Hernquist L., Cox T.J., Di Matteo T., Martini P., Robertson B., Springel V., 2005, *ApJ*, 630, 705
 Hopkins P.F., Hernquist L., Cox T.J., Di Matteo T., Robertson B., Springel V., 2006, *ApJS*, 163, 1
 Hopkins P.F., Hernquist L., Cox T.J., Kereš, D., 2008, *ApJS*, 175, 356
 Hopkins P.F., Kocevski D.D., Bundy K., 2014, *MNRAS*, 445, 823
 Kauffmann G., Haehnelt M., 2000, *MNRAS*, 311, 576
 Kocevski D., et al., 2012, *ApJ*, 744, 148
 Koutoulidis L., Plionis M., Georgantopoulos I., Fanidakis, N., 2013, *MNRAS*, 428, 1382
 La Franca F., et al., 2005, *ApJ*, 635, 864
 Leauthaud A., et al., 2015, *MNRAS*, 446, 1874
 Martini P., Weinberg D.H., 2001, *ApJ*, 547, 12
 Menci N., Fontana A., Giallongo E., Grazian A., Salimbeni S., 2006, *ApJ*, 647, 753
 Mendez A.J., et al., 2016, *ApJ*, 821, 55
 Merloni A., et al., 2014, *MNRAS*, 437, 3550
 Metropolis N., Rosenbluth A.W., Rosenbluth M.N., Teller A.H., Teller, E., 1953, *J. Chem. Phys.*, 21, 1087
 Netzer H., 2015, *ARA&A*, 53, 365
 Sanders D.B., Soifer B.T., Elias J.H., Madore B.F., Matthews K., Neugebauer G., Scoville N.Z., 1988, *ApJ*, 325, 74
 Sazonov S., Churazov E., Krivonos R., 2015, *MNRAS*, 454, 1202
 Springel V., Di Matteo T., Hernquist L., 2005, *MNRAS*, 361, 776
 Tinker J.L., Robertson B.E., Kravtsov A.V., Klypin A., Warren M.S., Yepes G., Gottlöber S., 2010, *ApJ*, 724, 878
 Treister E., Urry C.M., 2006, *ApJ*, 652, L79
 Treister E., Schawinski K., Urry C.M., Simmons B.D., 2012, *ApJ*,

758, L39

Tristram K.R.W., Burtscher L., Jaffe W., Meisenheimer K., Hönig S.F., Kishimoto M., Schartmann M., Weigelt G., 2014, *A&A*, 563, 82

Ueda Y., Akiyama M., Hasinger G., Miyaji T., Watson M.G., 2014, *ApJ*, 786, 104

Urry C.M., Padovani P., 1995, *PASP*, 107, 803

van den Bosch F.C., Yang X., Mo H.J., 2003, *MNRAS*, 340, 771

van den Bosch F., et al., 2007, *MNRAS*, 376, 841

Yang X., Mo H.J., van den Bosch, F., 2003, *MNRAS*, 339, 1057

APPENDIX A: A CHECK ON INTERNAL SELF-CONSISTENCY

A useful check on the measured CLF is to compute the luminosity-dependence of the mean Type 2 fraction, $\bar{f}_2(L)$, directly from the CLF using Eq. 13. Specific forms for $\bar{f}_2(L)$ are assumed during the computation of $f_2(L, M_h)$ (i.e., Eq. 16 or 17), but during the fit $f_2(L, M_h)$ is also subject to the requirement that it is bounded by unity at all L and M_h . Therefore, computing $\bar{f}_2(L)$ directly from Eq. 13 following the fit will provide a check on the self-consistency of the solution, as well as our assumption that $f_2(L, M_h)$ is separable into individual functions of L and M_h .

Both panels of Figure A1 compares $\bar{f}_2(L)$ computed from Eq. 13 directly (thin black solid lines) with the one input into the calculation (thick black lines). The hatched regions (bounded by the red lines) show the 95% confidence regions on the CLF-derived $\bar{f}_2(L)$, and the data points are the measurements on which the Eqs. 16 and 17 are based. The figure shows that at both redshifts the $\bar{f}_2(L)$ computed from the CLF model is consistent with both the observed Type 2 fractions and the input assumptions. More precise measurements of $f_2(L)$ will be important to improve the modeling of the Type 1 and Type 2 AGN CLFs.

This paper has been typeset from a $\text{\TeX}/\text{\LaTeX}$ file prepared by the author.

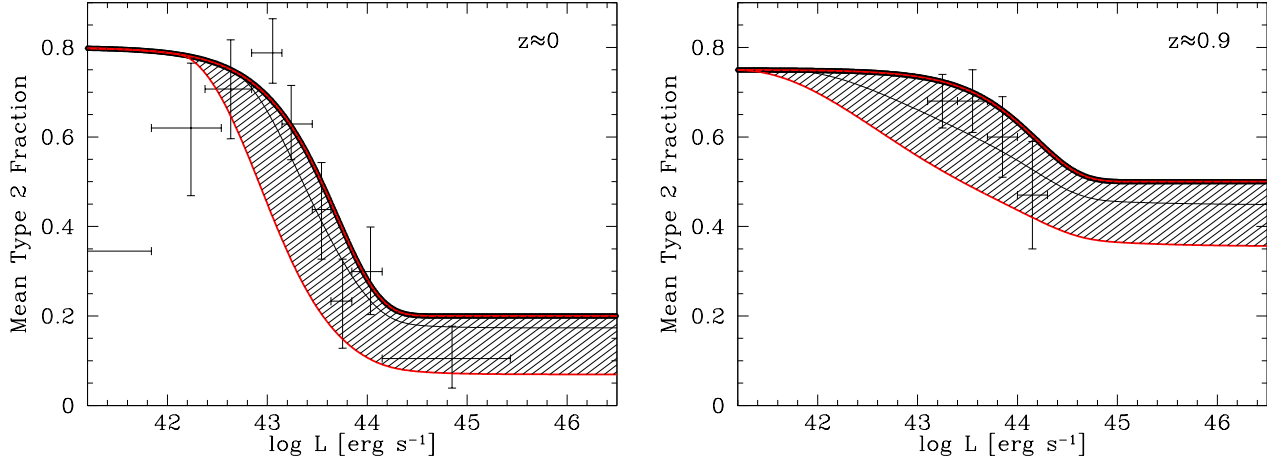


Figure A1. (Left) The mean Type 2 fraction versus AGN luminosity at $z \approx 0$. The thick black line plots the relation (Eq. 16) from Burlon et al. (2011) that was used as an input into the Type 2 and Type 1 CLF calculation (Sect. 2.2). The thin solid line and the hatched region plot the mean Type 2 fraction (and its 95% confidence region, bounded by the red lines) calculated from the best fit CLF model after fitting the data (Eq. 13). The data points show the *Swift*-BAT derived Type 2 fractions measured by Burlon et al. (2011). The mean Type 2 fractions calculated by the CLF model remains consistent with the Burlon et al. (2011) data and model. (Right) As in the left-hand panel, but now at $z \approx 0.9$. The thick black line plots Eq. 17 and the data points are the Type 2 fractions measured by Merloni et al. (2014) at $0.8 \leq z \leq 1.1$. Again, the CLF-derived mean Type 2 fractions are consistent with the input assumptions.